



Detection of CH₃C₃N in Titan's Atmosphere

Alexander E. Thelen^{1,2,9}, Martin A. Cordiner^{1,3}, Conor A. Nixon¹, Véronique Vuitton⁴, Zbigniew Kisiel⁵, Steven B. Charnley¹, Maureen Y. Palmer⁶, Nicholas A. Teanby⁷, and Patrick G. J. Irwin⁸

¹ Solar System Exploration Division, NASA Goddard Space Flight Center, Greenbelt, MD 20771, USA; alexander.e.thelen@nasa.gov

² Universities Space Research Association, Columbia, MD 21046, USA

³ Department of Physics, Catholic University of America, Washington, DC 20064, USA

⁴ Institut de Planétologie et d'Astrophysique de Grenoble, Université Grenoble Alpes, CNRS, F-38000 Grenoble, France

⁵ Institute of Physics, Polish Academy of Sciences, Al. Lotników 32/46, 02-668 Warszawa, Poland

⁶ Lunar and Planetary Laboratory, University of Arizona, Tucson, AZ 85721, USA

⁷ School of Earth Sciences, University of Bristol, Bristol BS8 1RJ, UK

⁸ Atmospheric, Oceanic and Planetary Physics, Clarendon Laboratory, University of Oxford, Oxford OX1 3PU, UK

Received 2020 September 22; revised 2020 October 15; accepted 2020 October 15; published 2020 November 2

Abstract

Titan harbors a dense, organic-rich atmosphere primarily composed of N₂ and CH₄, with lesser amounts of hydrocarbons and nitrogen-bearing species. As a result of high-sensitivity observations by the Atacama Large Millimeter/submillimeter Array (ALMA) in Band 6 (~230–272 GHz), we obtained the first spectroscopic detection of CH₃C₃N (methylcyanoacetylene or cyanopropyne) in Titan's atmosphere through the observation of seven transitions in the $J = 64 \rightarrow 63$ and $J = 62 \rightarrow 61$ rotational bands. The presence of CH₃C₃N on Titan was suggested by the Cassini Ion and Neutral Mass Spectrometer detection of its protonated form: C₄H₃NH⁺, but the atmospheric abundance of the associated (deprotonated) neutral product is not well constrained due to the lack of appropriate laboratory reaction data. Here, we derive the column density of CH₃C₃N to be $(3.8\text{--}5.7) \times 10^{12} \text{ cm}^{-2}$ based on radiative transfer models sensitive to altitudes above 400 km Titan's middle atmosphere. When compared with laboratory and photochemical model results, the detection of methylcyanoacetylene provides important constraints for the determination of the associated production pathways (such as those involving CN, CCN, and hydrocarbons), and reaction rate coefficients. These results also further demonstrate the importance of ALMA and (sub)millimeter spectroscopy for future investigations of Titan's organic inventory and atmospheric chemistry, as CH₃C₃N marks the heaviest polar molecule detected spectroscopically in Titan's atmosphere to date.

Unified Astronomy Thesaurus concepts: Saturnian satellites (1427); Natural satellites (Solar system) (1089); Radio astronomy (1338); Millimeter astronomy (1061); Radio spectroscopy (1359); Submillimeter astronomy (1647); Radiative transfer (1335); Planetary atmospheres (1244); Atmospheric composition (2120); Astrochemistry (75); Chemical abundances (224); Astronomical methods (1043)

1. Introduction

The atmosphere of Titan, the largest moon of Saturn, is primarily composed of N₂ (~95%–98%) and CH₄ (~1%–5%). A plethora of trace organic compounds makes up the remaining atmospheric composition, which are formed through the photo-dissociation of nitrogen and methane, and interactions with the Saturnian magnetosphere or galactic cosmic rays (GCRs; Loison et al. 2015; Vuitton et al. 2019). The formation of complex atmospheric species—such as nitriles (C_xH_y[CN]_z)—in Titan's upper atmosphere, their condensation and accumulation in the stratospheric haze layer, and participation in the methane-based meteorological cycle, are important processes that influence not only Titan's global climate but also the connection between the atmosphere and the organic regolith and hydrocarbon lakes. In addition to increasing our understanding of Titan's atmospheric and surface properties, knowledge of Titan's atmospheric photochemistry and the extent of its molecular inventory are important for assessing Titan's potential for habitability (Hörst et al. 2012; Palmer et al. 2017).

While numerous heavy ion species were detected with the Ion and Neutral Mass Spectrometer (INMS) and Cassini Plasma Spectrometer instruments on board the Cassini spacecraft at altitudes ~1000–1200 km, these measurements did not

fully resolve the identities of many large species—particularly those with a mass-to-charge ratio (m/z) > 60. Among these, the detection of ions with $m/z = 66$, attributed to C₄H₃NH⁺ (Vuitton et al. 2007), presented the case for multiple associated neutral species: CH₃C₃N (methylcyanoacetylene or cyanopropyne, hereafter the former) or H₂CCCHCN (cyanoallene). Laboratory experiments predict the formation of both C₄H₃N isomers in Titan's atmosphere through crossed molecular beam (Huang et al. 1999; Balucani et al. 2000) and plasma discharge (Thompson et al. 1991; Coll et al. 1999; Molina-Cuberos et al. 2002) experiments under Titan-like (N₂/CH₄-rich) conditions. However, while both methylcyanoacetylene and cyanoallene have been detected previously in the interstellar medium toward the Sgr B2 high-mass star-forming region and in the nearby molecular cloud TMC-1 (Broten et al. 1984; Lovas et al. 2006; Belloche et al. 2013), the C₄H₃N isomers have yet to be detected in the atmosphere of Titan.

The advent of the Atacama Large Millimeter/submillimeter Array (ALMA) in the past decade has enabled the exploration of Titan's atmospheric composition and dynamics to an unprecedented degree from the ground, allowing for follow-up studies on the distribution of trace molecular species by the Voyager 1 and Cassini–Huygens missions. Comprised of many 12 m antennas spatially separated by up to 16 km and access to frequencies ranging from ~84–950 GHz (~3.5–0.3 mm), ALMA has enabled the detection of new molecular species

⁹ NASA Astrobiology Postdoctoral Program Fellow.

(Cordiner et al. 2015; Palmer et al. 2017; Nixon et al. 2020), isotopes (Molter et al. 2016; Serigano et al. 2016; Thelen et al. 2019b; Iino et al. 2020), and vibrationally excited transitions (Cordiner et al. 2018; Kisiel et al. 2020) in Titan’s atmosphere. The spectral and spatial resolution capabilities of ALMA have also provided the means by which to map the distribution and dynamics of many nitrogen-bearing molecules (Cordiner et al. 2014, 2019; Lai et al. 2017; Lellouch et al. 2019; Thelen et al. 2019a), allowing for the study of atmospheric variations throughout Titan’s long (29.5 yr) seasonal cycle after the end of the Cassini mission in 2017.

Here, we detail the first results of deep ALMA Cycle 8 observations of Titan during 2019 November and December. The high sensitivity of these data have allowed for the spectroscopic detection of two $\text{CH}_3\text{C}_3\text{N}$ bands for the first time in Titan’s atmosphere (or indeed the atmosphere of any solar system body).

2. Observations

Titan was observed across multiple execution blocks between 2019 November 14 and December 16, under ALMA Project Code #2019.1.00783.S. Integrations on Titan were distributed across three Science Goals (SGs). SG1, which targeted the CO $J = 2 \rightarrow 1$ transition at 230.538 GHz to retrieve Titan’s disk-averaged temperature profile, was observed on 2019 November 14 for 11.59 minutes in ALMA configuration C43-3 (maximum baselines of 500 m) with 44 antennas. SG2 and SG3 covered multiple nitrile species, their C- and N-isotopes (e.g., H^{13}CCCN , HCCC^{15}N), and potential isocyanide species. Observations for these two Science Goals required seven executions between 2019 November 25 and December 16, with 43–45 antennas in ALMA configurations C43-1 and C43-2 (maximum baselines ranging from ~ 160 to 314 m); the cumulative integration time on Titan was 81.65 minutes for SG3 and 175.4 minutes for SG2, which required the highest spectral sensitivity (~ 1 mJy). Spectra from all three Science Goals were analyzed for the detection and subsequent radiative transfer modeling of CO and $\text{CH}_3\text{C}_3\text{N}$ transitions.

ALMA visibility data were calibrated with version 5.6.1-8 of the Common Astronomy Software Applications (CASA) pipeline using the scripts provided by the Joint ALMA Observatory (JAO). In addition to Titan, the quasars J1924–2914, J1911–2006, and J2056–4714 were also observed for the purposes of flux, bandpass, and phase calibrations. Subsequent executions of the pipeline calibrations were completed after modifying the JAO scripts to implement a variety of bandpass smoothing intervals to improve the spectral rms noise (particularly in SG2, with the longest total integration time) without significantly degrading the bandpass shape. See the Appendix for the results and discussion of the effects of bandpass smoothing on these ALMA observations.

The CASA `tclean` procedure was performed on the resulting calibrated visibility measurement sets to deconvolve the complex interferometric point-spread function (PSF) and reconstruct the brightness distribution of Titan in standard spatial coordinates. The Högbom algorithm was used during deconvolution with “natural” weighting applied to prioritize the image signal-to-noise ratio (S/N). The `tclean` image sizes and pixel scales were set to 270×270 $0''.16$ pixels for SG1, 224×224 $0''.17$ pixels for SG2, and 210×210 $0''.18$ pixels for SG3, so as to sufficiently sample the ALMA PSF

(~ 5 pixels across the FWHM). Images produced through concatenated integrations (SG2, SG3) were set to use a common synthesized beam shape (the ALMA PSF), and were corrected for the ALMA primary beam. The resulting images had beam sizes equal to $1''.276 \times 0''.933$ for SG1, $1''.470 \times 1''.067$ for SG2, and $1''.553 \times 1''.142$ for SG3. As Titan’s angular diameter (with its extended atmosphere up to 1200 km) was between $0''.954$ and $0''.985$ during these observations, we were unable to investigate potential spatial variation in the atmospheric distribution of $\text{CH}_3\text{C}_3\text{N}$ from these images. The resulting disk-averaged spectra of spectral windows (SPWs) 31 (SG2) and 37 (SG3) are shown in Figure 1, including the detections of the $\text{CH}_3\text{C}_3\text{N}$ $J = 64 \rightarrow 63$ ($S/N = 3.42\text{--}4.27\sigma$) and $J = 62 \rightarrow 61$ bands ($S/N = 2.37\text{--}4.58\sigma$), respectively, in the panel insets. The inherent channel spacing of the SG2 and SG3 spectral windows were 244 and 488 kHz, respectively, resulting in spectral resolutions of 488 and 976 kHz after Hanning smoothing by the correlator. A number of additional transitions from other molecular species were detected in these two spectral windows, which are detailed in Table 1. While the $\text{CH}_3\text{C}_3\text{N}$ $J = 62 \rightarrow 61$, $K = 2$ transition at 256.053 GHz was not detected above the noise in SG3 SPW 37, seven other $\text{CH}_3\text{C}_3\text{N}$ transitions were detected between both spectral windows (all but one of which were detected at greater than 3σ confidence level—see the Appendix).

3. Radiative Transfer Modeling and Results

Disk-averaged data were extracted from spectral image cubes using a circular mask that encompassed pixels with $\geq 90\%$ of Titan’s continuum flux (Lai et al. 2017; Thelen et al. 2019b; Nixon et al. 2020). Variations in Titan’s distance and relative velocity between integrations were accounted for in the previous calibration and imaging steps. We used 36 line-of-sight emission angles to properly characterize Titan’s disk-averaged radiance from the surface to 1200 km (Teanby et al. 2013; Thelen et al. 2018, 2019a), and applied small multiplicative factors to the spectra to resolve differences between the data and synthetic spectra in continuum regions (scaling factors on the order 1.15; see Thelen et al. 2018). We employed the Nonlinear optimal Estimator for Multi-variabE spectral analysis (NEMESIS) radiative transfer package (Irwin et al. 2008) to model Titan’s atmospheric emission and retrieve vertical temperature and volume mixing ratio profiles, as has been used previously for Cassini Composite Infrared Spectrometer and ALMA observations of Titan (see, for example, Nixon et al. 2010; Teanby et al. 2010). The NEMESIS atmospheric model parameterization we used follows the prescription of previous studies of Titan with ALMA (Thelen et al. 2018, 2019a, 2019b). Spectral line parameters from the Cologne Database for Molecular Spectroscopy (CDMS; Müller et al. 2001, 2005; Endres et al. 2016) were used for models of $\text{CH}_3\text{C}_3\text{N}$ (Moises et al. 1982; Bester et al. 1984, 1985; with purely K -dependent line parameters taken from CH_3CN , Anttila et al. 1993). The excited state $\text{C}_2\text{H}_5\text{CN}$ lines not yet available in CDMS (e.g., Figure 1, top inset) were taken from Kisiel et al. (2020). We assumed values for the $\text{CH}_3\text{C}_3\text{N}$ Lorentzian broadening half-width (Γ) = $0.115 \text{ cm}^{-1} \text{ bar}^{-1}$, and temperature dependence exponent (α) = 0.75, based on the N_2 -broadening parameters of CH_3CN (Dudaryonok et al. 2015) and C_3H_4 (Vinatier et al. 2007). As these coefficients are not well known for $\text{CH}_3\text{C}_3\text{N}$, we tested forward models over an

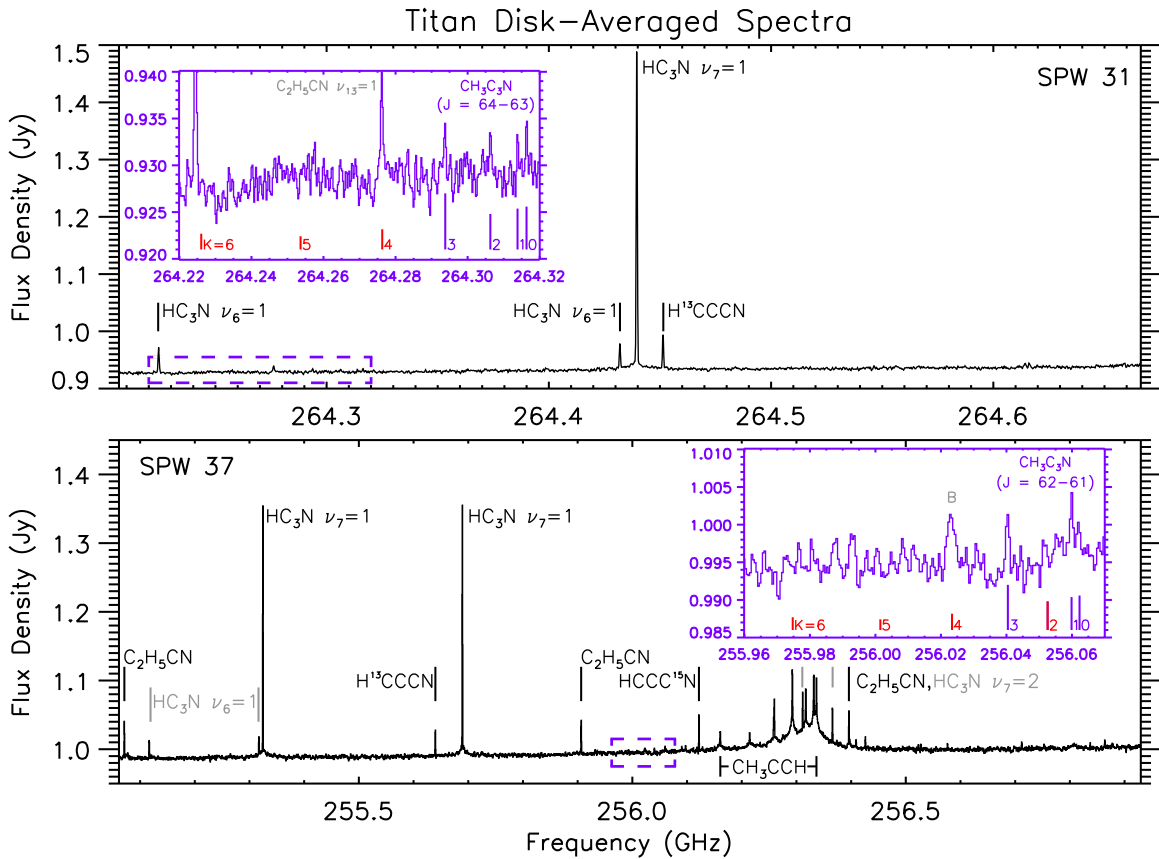


Figure 1. Disk-averaged spectra of Titan from SG2 and SG3 spectral windows 31 (top) and 37 (bottom), respectively. Strong spectral lines of various molecular species are marked with black or gray lines; spectral line parameters are detailed in Table 1. Additional unlabeled transitions of $\text{C}_2\text{H}_5\text{CN}$ and $\text{C}_2\text{H}_3\text{CN}$ are present. Insets in purple show the detections of the $\text{CH}_3\text{C}_3\text{N}$ $K = 0-3$ lines in the $J = 64 \rightarrow 63$ and $J = 62 \rightarrow 61$ bands. Both detected transitions (purple) and undetected or blended transitions (red) are marked, with marker heights proportional to the line intensities (calculated at 160 K). An additional, blended feature (B) is shown in the inset of SPW 37 at ~ 256.024 GHz, most likely a combination of C_3H_8 , $\text{C}_2\text{H}_5\text{CN}$, and $\text{CH}_3\text{C}_3\text{N}$.

appropriate parameter space [$\Gamma = 0.10-0.12 \text{ cm}^{-1} \text{ bar}^{-1}$; $\alpha = 0.65-0.85$], but found these changes had little effect ($<0.05\%$) on the model reduced- χ^2 values.

We first retrieved Titan’s disk-averaged temperature profile by modeling the $\text{CO } J = 2 \rightarrow 1$ transition from SG1 SPW 29 (Figure 2, top panel) by holding the CO vertical volume mixing ratio constant at 49.6 ppm due to the molecule’s long photochemical lifetime in Titan’s atmosphere (Serignano et al. 2016; Thelen et al. 2018). The a priori temperature profile was produced through a combination of the retrieved disk-averaged profile from ALMA observations of Titan in 2015 (Thelen et al. 2018) from lower stratospheric altitudes through the mesosphere ($\sim 100-600$ km), and from the Cassini radio-science and Huygens Atmospheric Structure Instrument temperature measurements in the troposphere (Fulchignoni et al. 2005; Schinder et al. 2012). The temperature profile was allowed to vary continuously throughout the atmosphere, with a priori uncertainties initially set to 5 K and a correlation length of 1.5 scale heights to sufficiently reduce artificial vertical oscillations in the retrieved profile. The resulting temperature profile is shown in Figure 2 (bottom panel), which was then used to model the $\text{CH}_3\text{C}_3\text{N}$ spectral bands from SG2 and SG3. As noted in previous ALMA studies, the (sub)millimeter lines of CO in Titan’s atmosphere allow for the measurement of temperature throughout the stratosphere and into the lower mesosphere, which is most notable in Figure 2 (bottom panel) where the retrieved temperature profile departs from the a priori

temperature profile at altitudes $\sim 100-530$ km ($\sim 10-10^{-3}$ mbar). Above 600 km, temperatures were set as an isothermal profile at 160 K.

As transitions from numerous other trace species are found in both SG2 and SG3 spectral windows containing $\text{CH}_3\text{C}_3\text{N}$ (Figure 1), we included the disk-averaged volume mixing ratio profiles of C_3H_4 , HC_3N (and its isotopes), and $\text{C}_2\text{H}_5\text{CN}$ from previous ALMA studies of Titan’s atmosphere (Cordiner et al. 2015; Lai et al. 2017; Thelen et al. 2019a) in models of $\text{CH}_3\text{C}_3\text{N}$ bands to correctly fit the continuum and contributions from nearby line wings. To mitigate the influence of these interloping species and best constrain the retrieved $\text{CH}_3\text{C}_3\text{N}$ mixing ratio profiles, we only modeled spectral regions covering the $K = 0-3$ transitions, as higher-energy lines were not detected in either $\text{CH}_3\text{C}_3\text{N}$ band. Due to the unknown nature (both in shape and relative abundance) of the vertical $\text{CH}_3\text{C}_3\text{N}$ mixing ratio profile, we attempted to fit both detected spectral bands with a variety of vertical profiles. Previous ALMA studies found that relatively narrow spectral lines (such as $\text{C}_2\text{H}_3\text{CN}$, $\text{C}_2\text{H}_5\text{CN}$, and $c\text{-C}_3\text{H}_2$) that sound Titan’s upper stratosphere and mesosphere could be adequately fit using vertical profiles consisting of constant mixing ratios above a certain altitude (step profiles), or profiles that are linear in log-pressure space (Cordiner et al. 2015; Palmer et al. 2017; Teanby et al. 2018; Nixon et al. 2020). Additionally, photochemical models of Titan’s atmosphere (Loison et al. 2015; Vuitton et al. 2019) make predictions for the vertical

Table 1
Spectral Transitions

Species	Rest Freq. (GHz)	Transition ^a	E'' (K)	SG	Spw
CO	230.538	$2 \rightarrow 1$	17	1	29
HC ₃ N	255.116	$28 \rightarrow 27, \nu_6 = 1f$	895	3	37
HC ₃ N	255.317	$28 \rightarrow 27, \nu_6 = 1e$	895	3	37
HC ₃ N	264.224	$29 \rightarrow 28, \nu_6 = 1e$	908	2	31
HC ₃ N	264.431	$29 \rightarrow 28, \nu_6 = 1f$	908	2	31
HC ₃ N	255.324	$28 \rightarrow 27, \nu_7 = 1f$	499	3	37
HC ₃ N	255.689	$28 \rightarrow 27, \nu_7 = 1e$	499	3	37
HC ₃ N	264.439	$29 \rightarrow 28, \nu_7 = 1e$	511	2	31
HC ₃ N	256.311	$28 \rightarrow 27, \nu_7 = 2f$	823	3	37
HC ₃ N	256.365	$28 \rightarrow 27, \nu_7 = 2e$	823	3	37
H ¹³ CCCN	255.639	$29 \rightarrow 28$	184	3	37
H ¹³ CCCN	264.451	$30 \rightarrow 29$	197	2	31
HCCC ¹⁵ N	256.121	$29 \rightarrow 28$	184	3	37
C ₂ H ₅ CN	255.071	$28_{2,26} \rightarrow 27_{2,25}$	182	3	37
C ₂ H ₅ CN	255.906	$28_{3,25} \rightarrow 27_{3,24}$	186	3	37
C ₂ H ₅ CN	256.396	$29_{1,28} \rightarrow 28_{1,27}$	189	3	37
C ₂ H ₅ CN	264.276	$29_{4,26} \rightarrow 28_{4,25}, \nu_{13} = 1$	502	2	31
CH ₃ CCH	256.097	$15_7 \rightarrow 14_7$	452	3	37
CH ₃ CCH	256.161	$15_6 \rightarrow 14_6$	358	3	37
CH ₃ CCH	256.214	$15_5 \rightarrow 14_5$	279	3	37
CH ₃ CCH	256.258	$15_4 \rightarrow 14_4$	214	3	37
CH ₃ CCH	256.293	$15_3 \rightarrow 14_3$	163	3	37
CH ₃ CCH	256.317	$15_2 \rightarrow 14_2$	127	3	37
CH ₃ CCH	256.332	$15_1 \rightarrow 14_1$	106	3	37
CH ₃ CCH	256.337	$15_0 \rightarrow 14_0$	98	3	37
<i>CH₃C₃N</i>	255.975	$62_6 \rightarrow 61_6$	656	3	37
<i>CH₃C₃N</i>	256.001	$62_5 \rightarrow 61_5$	574	3	37
<i>CH₃C₃N</i>	256.023	$62_4 \rightarrow 61_4$	507	3	37
CH ₃ C ₃ N	256.040	$62_3 \rightarrow 61_3$	455	3	37
<i>CH₃C₃N</i>	256.053	$62_2 \rightarrow 61_2$	417	3	37
CH ₃ C ₃ N	256.060	$62_1 \rightarrow 61_1$	395	3	37
CH ₃ C ₃ N	256.062	$62_0 \rightarrow 61_0$	387	3	37
<i>CH₃C₃N</i>	264.226	$64_6 \rightarrow 63_6$	682	2	31
<i>CH₃C₃N</i>	264.254	$64_5 \rightarrow 63_5$	599	2	31
<i>CH₃C₃N</i>	264.276	$64_4 \rightarrow 63_4$	532	2	31
CH ₃ C ₃ N	264.294	$64_3 \rightarrow 63_3$	480	2	31
CH ₃ C ₃ N	264.306	$64_2 \rightarrow 63_2$	442	2	31
CH ₃ C ₃ N	264.314	$64_1 \rightarrow 63_1$	420	2	31
CH ₃ C ₃ N	264.316	$64_0 \rightarrow 63_0$	412	2	31

Notes. Rows in italics denote undetected (often higher-energy) CH₃C₃N transitions. CH₃C₃N line positions were taken from the CDMS catalog.

^a Rotational transitions are written as $J'' \rightarrow J', J''_{K''} \rightarrow J'_{K'}$, or $J''_{K''_a, K''_c} \rightarrow J'_{K'_a, K'_c}$.

profile of CH₃C₃N and other trace species, which can then be tested through radiative transfer modeling. As the spectral resolution in these ALMA observations are relatively high and include few spectral lines, we ran NEMESIS in the more accurate line-by-line mode as opposed to utilizing the correlated- k method as is done for infrared and visible wavelengths. We fit both spectral windows separately for independent confirmation of the retrieved CH₃C₃N volume mixing ratio profiles, and in all cases found the resulting mixing ratios between the two spectral windows to agree within the 1σ retrieval errors. We report the final volume mixing ratios as a weighted mean of each pair of retrievals; the rms of our SG2 data is $\sim\sqrt{2}$ less than that of SG3 (see the Appendix). A variety of synthetic model spectra corresponding to the vertical profile retrievals detailed below are shown for both bands of

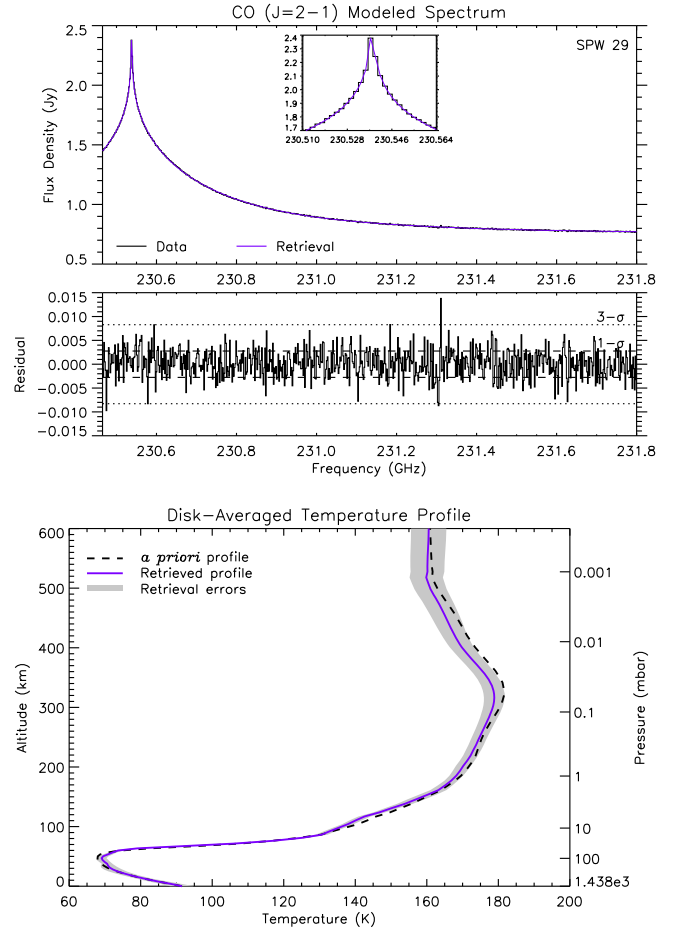


Figure 2. (Top) ALMA disk-averaged spectrum (black) of the CO $J = 2 \rightarrow 1$ transition, with the best-fit NEMESIS model after retrieving Titan’s vertical temperature profile (purple). The residual (data minus model) spectrum is shown below with 1σ (dashed) and 3σ (dotted) rms values. (Bottom) The corresponding retrieved temperature profile (purple) and error envelope (gray). The a priori temperature profile is shown (dashed black) from previous ALMA and Cassini observations.

CH₃C₃N in Figures 3(A) and (B), with the weighted-mean best-fit profiles shown in Figure 3(C) compared to the photochemical model of Loison et al. (2015). The retrieved abundances and calculated column densities for these profiles are detailed in Table 2.

First, we attempted to fit both CH₃C₃N spectral bands with a range of step profiles from 100–800 km with uniform mixing ratio at every 100 km interval, initially set at a test value of 2.5 ppb. Profiles were then scaled iteratively by NEMESIS until converging upon a fit that sufficiently minimized the reduced- χ^2 value, which was found to be similar for all step profiles above 400 km (Table 2). Below these altitudes, the synthetic CH₃C₃N line wings contribute too much to obtain a good fit (i.e., $\chi^2/n > 1$); an example is shown in Figures 3(A) and (B) for a 300 km step model (red spectrum). Between 400 and 800 km, the spectral fits do not differ significantly (Table 2). Here, we find the total integrated column density of CH₃C₃N to range between $(3.86\text{--}5.73) \times 10^{12} \text{ cm}^{-2}$ from the best-fit step models (Figure 3(C), orange dashed lines).

Next, a linear gradient was parameterized by allowing NEMESIS to vary the volume mixing ratio and pressure between two points, with zero abundance below the high-pressure point (Point 1, with pressure p_1 and mixing ratio q_1)

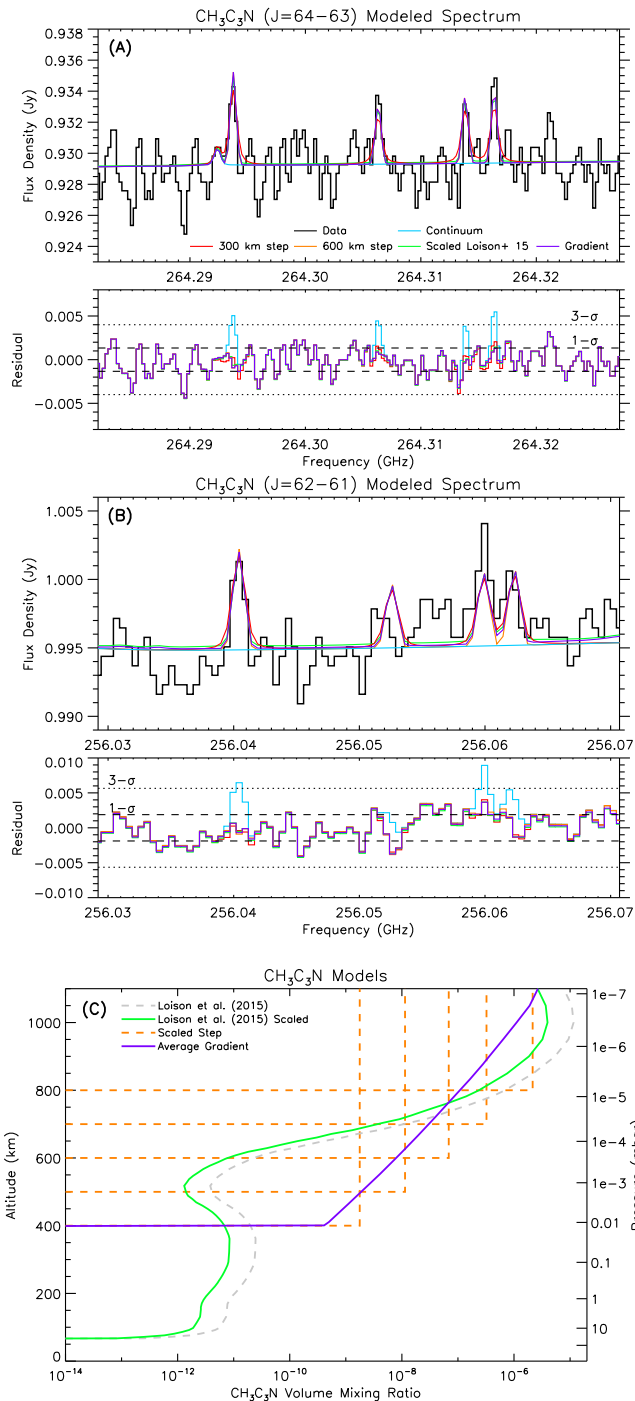


Figure 3. (A) Disk-averaged spectrum of $\text{CH}_3\text{C}_3\text{N}$ $J = 64 \rightarrow 63$ (black) compared to various NEMESIS synthetic spectra (colored lines). The residual (data minus model) spectra are shown below with 1σ (dashed) and 3σ (dotted) rms values. A transition of $\text{C}_2\text{H}_5\text{CN}$ is included in the model at ~ 264.292 GHz. (B) The $\text{CH}_3\text{C}_3\text{N}$ $J = 62 \rightarrow 61$ band with modeled spectra, as in (A). (C) The weighted-mean best-fit vertical profiles of Titan’s $\text{CH}_3\text{C}_3\text{N}$ volume mixing ratio as retrieved with NEMESIS from spectra in (A) and (B) (green, orange, and purple lines). The nominal photochemical model of Loison et al. (2015) is shown for comparison (dashed gray).

and constant abundance above the low-pressure point (Point 2, with pressure p_2 and mixing ratio q_2). While the p_1 and q_1 values were initially set with fairly arbitrary values with large errors to allow flexibility in the profile to achieve a good fit, p_2 and q_2 were set to be constrained by the INMS measurements of $\text{C}_4\text{H}_3\text{NH}^+$ ions in Titan’s upper atmosphere (~ 1100 km),

Table 2
 $\text{CH}_3\text{C}_3\text{N}$ Best-fit Model Results

Model	χ^2/n^a	VMR ^b	N (cm^{-2}) ^c
400 km Step	1.035	$(1.771 \pm 0.196) \times 10^{-09}$	5.727×10^{12}
500 km Step	1.020	$(1.139 \pm 0.120) \times 10^{-08}$	4.723×10^{12}
600 km Step	1.018	$(6.851 \pm 0.693) \times 10^{-08}$	4.400×10^{12}
700 km Step	1.018	$(3.230 \pm 0.312) \times 10^{-07}$	3.860×10^{12}
800 km Step	1.018	$(2.152 \pm 0.198) \times 10^{-06}$	5.607×10^{12}
Linear Gradient	1.019		4.709×10^{12}
Point 1 (400 km)		$(4.093 \pm 0.339) \times 10^{-10}$	
Point 2 (1100 km)		$(2.675 \pm 0.222) \times 10^{-06}$	
Loison et al. (2015) Scaling	0.978	0.343 ± 0.115	9.741×10^{12}

Notes.

^a Reduced- χ^2 values, where n = number of data points minus model degrees of freedom.

^b Retrieved volume mixing ratios (VMRs) are presented for all models except the scaling retrieval of the Loison et al. (2015) model, where the scale factor and error are shown. The VMR values for the two (high and low) pressure point fits of the linear gradient model are listed.

^c Total column density integrated up to 1200 km.

with the inferred neutral $\text{C}_4\text{H}_3\text{N}$ volume mixing ratio ranging between $(2\text{--}4) \times 10^{-6}$ (Vuitton et al. 2007, 2019). Here, $\text{CH}_3\text{C}_3\text{N}$ lines were only sensitive to abundance above 400 km ($p_1 = 1.19 \times 10^{-2}$ mbar), resulting in $q_1 = 0.41$ ppb and $q_2 = 2.68$ ppm at 1100 km ($p_2 = 7.64 \times 10^{-8}$ mbar). The resulting synthetic spectra and gradient profile are shown in Figure 3 (purple lines). The integrated column density of this linear gradient model is $4.71 \times 10^{12} \text{ cm}^{-2}$, in broad agreement with the step model profiles.

Finally, we attempted to fit the spectra by retrieving a multiplicative scaling factor applied to the photochemical model profile of Loison et al. (2015). This profile produced a good fit when scaled by a factor of 0.34 of the original nominal model (Figures 3(A) and (B), green spectra; Figure 3(C), green line). The resulting column density of $9.74 \times 10^{12} \text{ cm}^{-2}$, however, is higher than that of the best-fit step or gradient models by a factor of $\sim 1.7\text{--}2.5$ (Table 2).

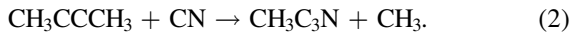
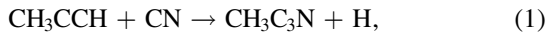
4. Discussion and Conclusions

Though we were able to fit both detected $\text{CH}_3\text{C}_3\text{N}$ spectral bands with a variety of vertical profiles (Figure 3(C)), the relatively short photochemical lifetime of $\text{CH}_3\text{C}_3\text{N}$ —between 10^4 and 10^6 s from 400 to 800 km (Loison et al. 2015)—suggests that a vertically uniform mixing ratio profile may not be physically realistic. As such, the scaled profile of Loison et al. (2015) and linear gradient (Figure 3(C), green and purple lines, respectively) are favored for the volume mixing ratio profile of $\text{CH}_3\text{C}_3\text{N}$. These profiles depict the formation of $\text{CH}_3\text{C}_3\text{N}$ in Titan’s upper atmosphere 400–500 km (similar to its protonated counterpart, $\text{C}_4\text{H}_3\text{NH}^+$) with decreasing abundance as a function of depth as the result of photodissociation and lack of reactive radicals (such as CN and CCN). The dissociation of $\text{CH}_3\text{C}_3\text{N}$ has yet to be studied in detail, though the pathways $\text{CH}_2\text{C}_3\text{N} + \text{H}$ or $\text{CH}_3 + \text{C}_3\text{N}$ have been suggested by Loison et al. (2015); alternatively, by analogy with HC_3N (see Huebner & Mukherjee 2015; Vuitton et al. 2019), we might expect that $\text{CH}_3\text{C}_3\text{N}$ photolysis instead yields CH_3C_2 and CN. We find insufficient $\text{CH}_3\text{C}_3\text{N}$ abundance at altitudes < 400 km to properly identify the dependence of the

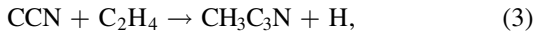
mixing ratio on altitude in Titan’s stratosphere and below, where GCR chemistry may play an additional role in complex molecule formation.

Our retrieved volume mixing ratios above 700 km (Table 2) are in good agreement with the estimated $\text{CH}_3\text{C}_3\text{N}$ upper limit of 2.5×10^{-7} by Cerceau et al. (1985) based on the derived stratospheric HCN and HC_3N abundances in Titan’s north pole (then in winter) from Voyager 1 infrared measurements. Further, the derived column densities from this work between $(3.8\text{--}5.7) \times 10^{12} \text{ cm}^{-2}$ are in agreement with the lower value of $5.5 \times 10^{12} \text{ cm}^{-2}$ found in the laboratory simulations by Coll et al. (1999). The scaling of the nominal Loison et al. (2015) profile by a factor of 0.34 places it within 50% of their simulated profiles (see their Figure 14), which show significant spread due to the unknown reaction rate coefficients for the production and loss of $\text{CH}_3\text{C}_3\text{N}$. The linear gradient low-pressure point (q_2), 800 km step, and scaled profile of the Loison et al. (2015) model results here are all in agreement with the inferred $\text{C}_4\text{H}_3\text{N}$ volume mixing ratio of 2×10^{-6} at 1100 km from the Cassini T40 flyby INMS measurements by Vuitton et al. (2019).

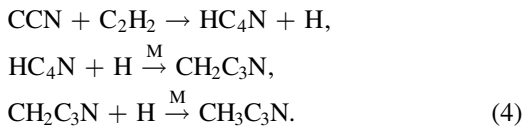
While the Loison et al. (2015) $\text{CH}_3\text{C}_3\text{N}$ model corroborates the upper atmospheric abundance of $\text{C}_4\text{H}_3\text{N}$ inferred by Vuitton et al. (2007) from the T5 INMS measurements (a factor of 2 higher than those derived from T40 in Vuitton et al. 2019), a large disparity between the photochemical models (and within the ensemble of models produced by Loison et al. 2015) arises in the lower atmosphere due to the poorly constrained $\text{C}_4\text{H}_3\text{N}$ branching ratios and reaction rate coefficients at temperatures appropriate for Titan. Aside from electron dissociative recombination of $\text{C}_4\text{H}_3\text{NH}^+$ (Vuitton et al. 2007), neutral production of $\text{CH}_3\text{C}_3\text{N}$ can occur in a few ways, as found through crossed beam experiments and theoretical and photochemical modeling studies (Huang et al. 1999; Balucani et al. 2000; Zhu et al. 2003; Wang et al. 2006; Loison et al. 2015). First, through the reactions of larger hydrocarbons with CN radicals,



Similarly, with CCN radicals following their formation through $\text{H} + \text{HCCN}$ (Takayanagi et al. 1998; Osamura & Petrie 2004) and subsequent reactions with ethylene,



or through the chain beginning with acetylene,



While both reactions (3) and (4) are found to be equally likely by Loison et al. (2015), the production of CCN via $\text{H} + \text{HCCN}$ is not well constrained, and the synthesis of $\text{CH}_3\text{C}_3\text{N}$ through CN radicals (Equations (1) and (2)) are not included in their photochemical model. Additionally, cyanoallene may be produced through reactions (1)–(4) instead of (or in addition to) methylcyanoacetylene. $\text{CH}_3\text{C}_3\text{N}$ itself may form the protonated species, $\text{C}_4\text{H}_3\text{NH}^+$, through reactions with the HCNH^+ and C_2H_5^+ ions producing HCN and C_2H_4 , respectively (Vuitton et al. 2007). The other mechanism for forming

$\text{C}_4\text{H}_3\text{NH}^+$ is through the combination of HCN and $1\text{-C}_3\text{H}_3^+$, though the reaction rate coefficient for this reaction and the abundance of $1\text{-C}_3\text{H}_3^+$ are unknown (Vuitton et al. 2007). As such, the production and loss pathways for both $\text{C}_4\text{H}_3\text{NH}^+$ and $\text{CH}_3\text{C}_3\text{N}$ require further investigation.

The detection of $\text{CH}_3\text{C}_3\text{N}$ here supports the previous identification of $\text{C}_4\text{H}_3\text{NH}^+$ at $m/z = 66$ from Cassini/INMS observations, and adds a valuable component to Titan’s extensive atmospheric photochemistry while revealing the need for further laboratory and photochemical model studies detailing the production and dissociation of Titan’s larger nitriles. The retrieved column density and upper atmospheric abundances agree with previous INMS measurements and laboratory and photochemical model predictions, though the lack of sensitivity to Titan’s lower atmosphere through the $J = 64 \rightarrow 63$ and $J = 62 \rightarrow 61$ rotational bands inhibits our investigation of the stratospheric volume mixing ratio and condensation of $\text{CH}_3\text{C}_3\text{N}$. However, these results provide insights into the possible shape of the full vertical profile through the scaling of the model produced by Loison et al. (2015), and place constraints on the total column density of $\text{CH}_3\text{C}_3\text{N}$ in Titan’s atmosphere to aid in the determination of the production ratio of methylcyanoacetylene to cyanoallene, and the abundance of products resulting from the photodissociation both species. The detection of $\text{CH}_3\text{C}_3\text{N}$ also provides the incentive for future observations of Titan at long wavelengths in the pursuit of further complex, polar nitriles (such as $\text{C}_3\text{H}_7\text{CN}$ and HC_5N) that are predicted to exist in Titan’s atmosphere. Finally, as with other trace species with fairly short photochemical lifetimes (compared to dynamical timescales), $\text{CH}_3\text{C}_3\text{N}$ may have a complex and temporally variable spatial distribution that can be investigated with ALMA in the future through higher angular resolution observations.

The authors would like to thank N. Chanover, M. Dobrijevic, and J. C. Loison for their previous efforts in the proposed ALMA observations targeting $\text{CH}_3\text{C}_3\text{N}$ and other molecules in Titan’s atmosphere, and R. Cosentino and E. Villard for discussions regarding ALMA bandpass smoothing.

A.E.T. was supported by the NASA Astrobiology Postdoctoral Program in association with the NASA Astrobiology Institute (NAI) and the Universities Space Research Association. M.A.C. was funded by the National Science Foundation Grant #AST-1613987. C.A.N. and M.A.C. received funding from NASA’s Solar System Observations Program. C.A.N. was supported by the NAI. N.A.T. and P.G.J.I. were funded by the UK Science and Technology Facilities Council.

This Letter makes use of the following ALMA data: ADS/JAO.ALMA#2019.1.00783.S. ALMA is a partnership of ESO (representing its member states), NSF (USA) and NINS (Japan), together with NRC (Canada) and NSC and ASIAA (Taiwan) and KASI (Republic of Korea), in cooperation with the Republic of Chile. The Joint ALMA Observatory is operated by ESO, AUI/NRAO and NAOJ. The National Radio Astronomy Observatory is a facility of the National Science Foundation operated under cooperative agreement by Associated Universities, Inc.

Appendix Application of ALMA Bandpass Smoothing

Bandpass calibration is practiced in radio and (sub)millimeter observations through the use of an off-source target to remove frequency (and sometimes time) dependent fluctuations in

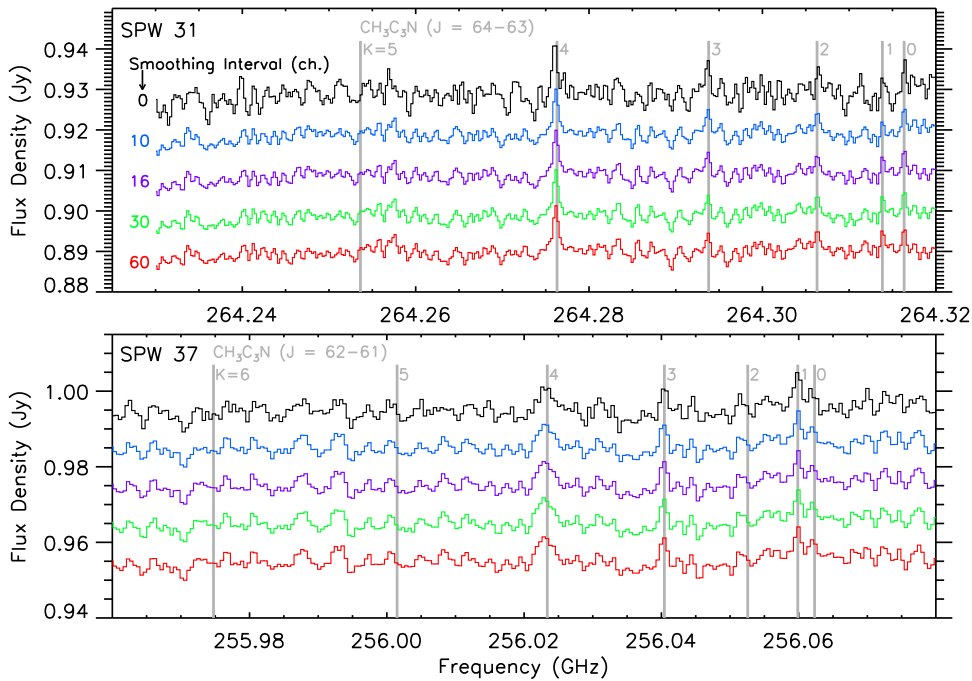


Figure 4. (Top) Disk-averaged Titan spectra from spectral window 31 showing the effects of various bandpass smoothing intervals: 0 (black, default), 10 (blue), 16 (purple), 30 (green), and 60 channels (red). Spectra are separated by 10 mJy for visibility. Transitions of the $\text{CH}_3\text{C}_3\text{N}$ $J = 64 \rightarrow 63$ band are marked in gray. Spectral lines with significant flux (e.g., HC_3N $\nu_6 = 1$) were removed for clarity (see Figure 1 and Table 1). (Bottom) Spectra are shown as in the top panel, but for SPW 37. Smoothing was applied for the same number of channel intervals, and denoted by the same colors as the top panel. Transitions of $\text{CH}_3\text{C}_3\text{N}$ $J = 62 \rightarrow 61$ are marked in gray.

visibility amplitudes and phases across spectral windows, which often manifest as continuum ripples or undulations in target spectra. Proper bandpass calibration can increase the dynamic range of (sub)millimeter images, and facilitates the measurement of weak (or broad) spectroscopic features. Often, quasi-stellar objects with well-characterized properties are observed for short durations (typically 2–30 minutes) with ALMA to remove visibility artifacts as a function of frequency, which improves variations in amplitude and phase to $\lesssim 0.1\%$ and $\lesssim 0.3$ deg in ALMA Bands 3–6, respectively (though edge channels are still routinely removed due to large amplitude changes).

It has been shown that noise from variations in frequency in the bandpass calibration solution can approach system noise (i.e., random noise in radio antenna receivers) for short bandpass calibrator integrations, but the application of bandpass smoothing (applied to the calibration target solution) or additional calibrator integration time can further reduce the total spectral rms through the reduction of bandpass artifacts (Yamaki et al. 2012). This has been demonstrated to be effective for ALMA as well for spectral intervals with $\Delta\nu < 100$ MHz.¹⁰ As such, though the total integration time of SG2 was a factor ~ 2 more than that of SG3 in our observations (see Section 2), the corresponding spectral noise was not initially decreased by $\sim\sqrt{2}$ due to the limitations of noise from the default bandpass calibrator solutions. Here, we varied the bandpass solution interval to apply smoothing to the bandpass calibration function by averaging over a range of channels. Figure 4 shows the resulting disk-averaged spectra for SPW 31 and SPW 37 after using between 0 and 60 channel bandpass smoothing solutions. Here, the effects of bandpass

smoothing are particularly evident in the comparison between 0 and 10–30 channel solution intervals.

We found that after applying a smoothing interval of 16 channels (7.81 MHz in SG2 SPW 31, 15.6 MHz in SG3 SPW 37) the rms decreased by a factor of 1.67 in SPW 31 and by a factor of 1.12 in SPW 37 (Figure 5(A)). The resulting rms in SPW 31 (1.33 mJy) was then a factor of $\sim\sqrt{2}$ less than in SPW 37 (1.88 mJy). Additionally, the decrease in spectral noise from the $\text{CH}_3\text{C}_3\text{N}$ bands reduced the apparent peak line flux density of some transitions by $\sim 1\sigma$, but the corresponding decrease in rms improved the overall S/N in most lines of both spectral bands (Figures 5(B) and (C)). An example of the removal of additive noise peaks from spectral line fluxes after bandpass smoothing is shown in Figure 6. We found that 16 channel smoothing resulted in the optimal increase in S/N across all lines of both spectral bands for $\text{CH}_3\text{C}_3\text{N}$. Increased smoothing (>20 – 30 MHz) showed diminishing returns on spectral rms, though caution should be taken when averaging over large intervals, as the continuum may be adversely affected—particularly for channels close to either edge of the bandwidth (Figure 6, red spectrum). The optimal channel interval depends on spectral resolution, frequency, bandpass, and target integration time, so we encourage observers to experiment with multiple bandpass smoothing solutions to determine the appropriate solution interval for observations with ALMA.

The application of bandpass smoothing in radio spectra has previously been studied by Yamaki et al. (2012) with similar results in rms improvements after increased channel smoothing intervals and additional time on bandpass calibration sources. To facilitate the detection of additional trace gases in planetary atmospheres, bandpass smoothing may be applied to ALMA

¹⁰ See ALMA Technical Notes 15 (https://almascience.org/documents-and-tools/alma-technical-notes/ALMATechnicalNotes15_FINAL.pdf/view).

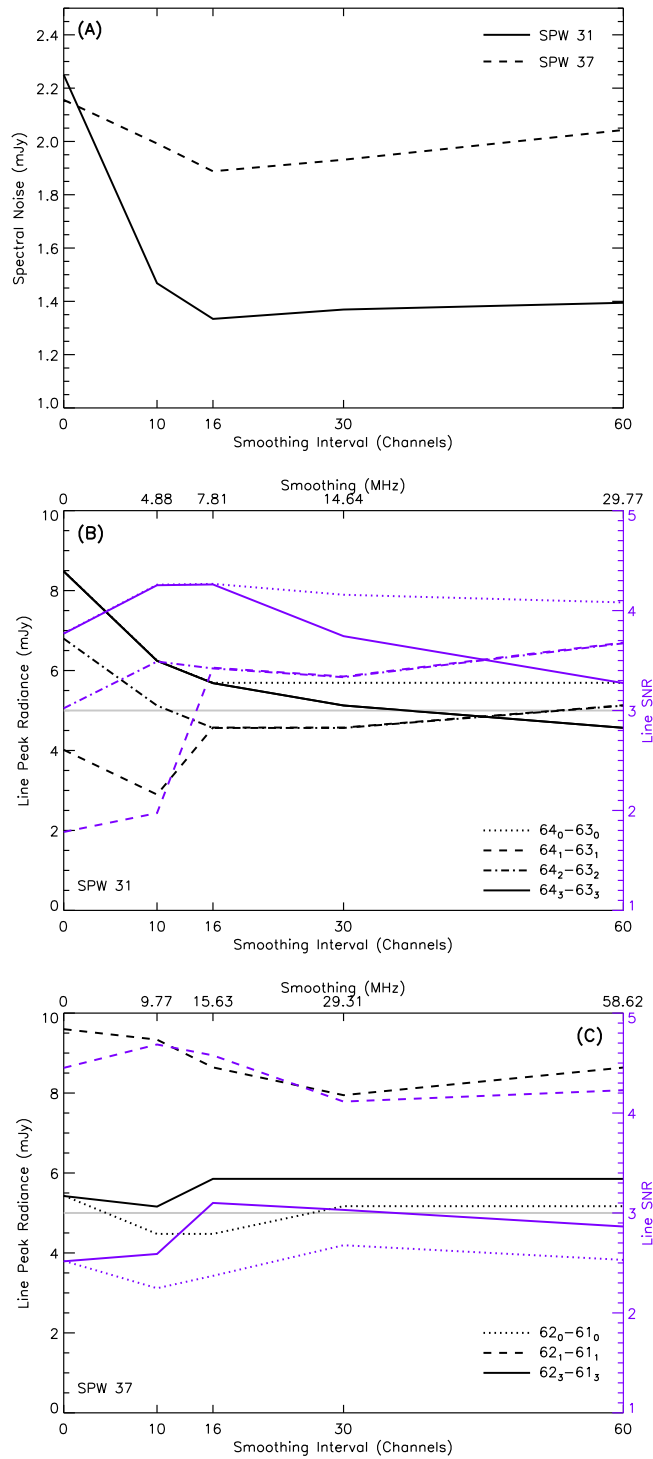


Figure 5. (A) The response of the rms noise in spectral windows 31 (solid) and 37 (dashed) as a function of bandpass smoothing interval in channels. (B) The calculated line peak flux (line minus continuum) as a function of smoothing interval for all four detected $\text{CH}_3\text{C}_3\text{N}$ transitions in SPW 31 (black lines) and the resulting signal-to-noise ratio (purple lines and corresponding y-axis) when divided by the rms values in (A). The 3σ threshold is marked in gray for reference. (C) Same as (B), but for SPW 37. The $\text{CH}_3\text{C}_3\text{N}$ $J = 62_2 \rightarrow 61_2$ transition is not plotted here, as the line flux remained at the noise level for all bandpass smoothing intervals (Figures 3(B) and 4).

data with long integration times. Here, we find limited increase in line S/N for SG3 (Figures 5(A) and (C)), similar to previous efforts to detect $\text{c-C}_3\text{H}_2$ in ALMA observations of Titan (Nixon et al. 2020); however, the significant decrease in rms in SG2 (Figures 5(A) and (B)) promotes the use of bandpass

smoothing for Titan observations with total (on-source) integration times of $\gtrsim 2$ hr. Additionally, increased integration time on bandpass calibrators, which is available under specific well-justified conditions by ALMA, may further decrease the spectral rms (Yamaki et al. 2012).

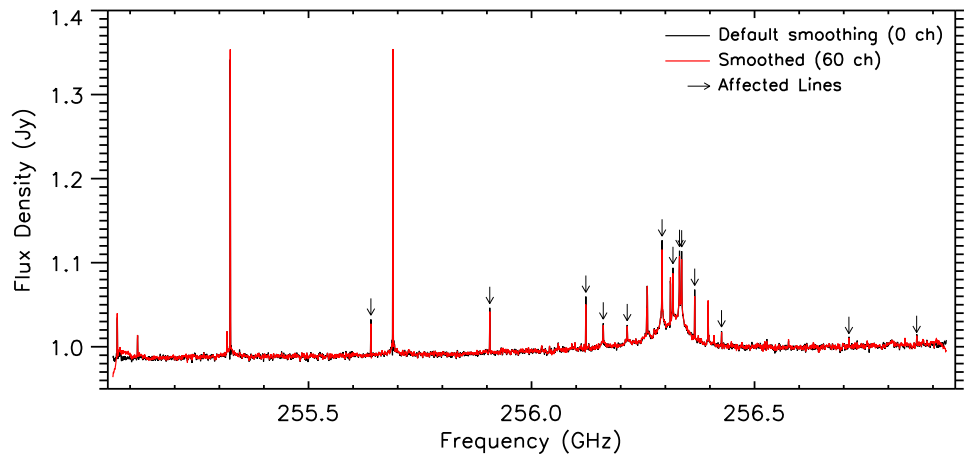


Figure 6. Comparison of disk-averaged Titan spectra from SG3 (SPW 37) with default (black) and 60 channel bandpass smoothing (red) applied. Transitions with reduced apparent line peak fluxes after the decrease of rms noise as a result of bandpass smoothing are marked with arrows. Bandpass artifacts induced by excessive smoothing are apparent toward the bandwidth edges (red spectrum <255.15 and >256.9 GHz).

ORCID iDs

Alexander E. Thelen  <https://orcid.org/0000-0002-8178-1042>

Martin A. Cordiner  <https://orcid.org/0000-0001-8233-2436>

Conor A. Nixon  <https://orcid.org/0000-0001-9540-9121>

Véronique Vuitton  <https://orcid.org/0000-0001-7273-1898>

Zbigniew Kisiel  <https://orcid.org/0000-0002-2570-3154>

Maureen Y. Palmer  <https://orcid.org/0000-0001-9132-5588>

Nicholas A. Teanby  <https://orcid.org/0000-0003-3108-5775>

Patrick G. J. Irwin  <https://orcid.org/0000-0002-6772-384X>

References

- Anttila, R., Horneman, V., Koivusaari, M., & Paso, R. 1993, *JMoSp*, **157**, 198
 Balucani, N., Asvany, O., Osamura, Y., et al. 2000, *P&SS*, **48**, 447
 Belloche, A., Müller, H. S. P., Menten, K. M., Schilke, P., & Comito, C. 2013, *A&A*, **559**, A47
 Bester, M., Tanimoto, M., Vowinkel, B., Winnewisser, G., & Yamada, K. 1985, *ZNatA*, **38**, 64
 Bester, M., Yamada, K., Winnewisser, G., et al. 1984, *A&A*, **137**, L20
 Broten, N. W., MacLeod, J. M., Avery, L. W., et al. 1984, *ApJL*, **276**, L25
 Cerceau, F., Raulin, F., Courtin, R., & Gautier, D. 1985, *Icar*, **62**, 207
 Coll, P., Coscia, D., Smith, N., et al. 1999, *P&SS*, **47**, 1331
 Cordiner, M. A., Nixon, C. A., Chamley, S. B., et al. 2018, *ApJL*, **859**, L15
 Cordiner, M. A., Nixon, C. A., Teanby, N. A., et al. 2014, *ApJL*, **795**, L30
 Cordiner, M. A., Palmer, M. Y., Nixon, C. A., et al. 2015, *ApJL*, **800**, L14
 Cordiner, M. A., Teanby, N. A., Nixon, C. A., et al. 2019, *AJ*, **158**, 76
 Dudaryonok, A. S., Lavrentieva, N. N., & Buldyreva, J. V. 2015, *Icar*, **256**, 30
 Endres, C. P., Schlemmer, S., Schilke, P., Stutzki, J., & Müller, H. S. P. 2016, *JMoSp*, **327**, 95
 Fulchignoni, M., Ferri, F., Angrilli, F., et al. 2005, *Natur*, **438**, 785
 Hörst, S. M., Yelle, R. V., Buch, A., et al. 2012, *AsBio*, **12**, 809
 Huang, L. C. L., Balucani, N., Lee, Y. T., Kaiser, R. I., & Osamura, Y. 1999, *JChPh*, **111**, 2857
 Huebner, W., & Mukherjee, J. 2015, *P&SS*, **106**, 11
 Iino, T., Sagawa, H., & Tsukagoshi, T. 2020, *ApJ*, **890**, 95
 Irwin, P. G. J., Teanby, N. A., de Kok, R., et al. 2008, *JQSRT*, **109**, 1136

- Kisiel, Z., Nixon, C. A., Cordiner, M. A., Thelen, A. E., & Chamley, S. B. 2020, *JMoSp*, **372**, 111324
 Lai, J. C.-Y., Cordiner, M. A., Nixon, C. A., et al. 2017, *AJ*, **154**, 206
 Lellouch, E., Gurwell, M. A., Moreno, R., et al. 2019, *NatAs*, **3**, 614
 Loison, J. C., Hébrard, E., Dobrijevic, M., et al. 2015, *Icar*, **247**, 218
 Lovas, F. J., Remijan, A. J., Hollis, J. M., Jewell, P. R., & Snyder, L. E. 2006, *ApJL*, **637**, L37
 Moïses, A., Boucher, D., Burie, J., Demaison, J., & Dubrulle, A. 1982, *JMoSp*, **92**, 497
 Molina-Cuberos, G. J., Schwingenschuh, K., López-Moreno, J. J., et al. 2002, *JGRE*, **107**, 5099
 Molter, E. M., Nixon, C. A., Cordiner, M. A., et al. 2016, *AJ*, **152**, 42
 Müller, H. S. P., Schlöder, F., Stutzki, J., & Winnewisser, G. 2005, *JMoSt*, **742**, 215
 Müller, H. S. P., Thorwirth, S., Roth, D. A., & Winnewisser, G. 2001, *A&A*, **370**, L49
 Nixon, C. A., Achterberg, R. K., Teanby, N. A., et al. 2010, *FaDi*, **147**, 65
 Nixon, C. A., Thelen, A. E., Cordiner, M. A., et al. 2020, *AJ*, **160**, 205
 Osamura, Y., & Petrie, S. 2004, *JPCA*, **108**, 3615
 Palmer, M. Y., Cordiner, M. A., Nixon, C. A., et al. 2017, *SciA*, **3**, e1700022
 Schinder, P. J., Flasar, F. M., Marouf, E. A., et al. 2012, *Icar*, **221**, 1020
 Serigano, J., Nixon, C. A., Cordiner, M. A., et al. 2016, *ApJL*, **821**, L8
 Takayanagi, T., Kurosaki, Y., Misawa, K., et al. 1998, *JPCA*, **102**, 6251
 Teanby, N. A., Cordiner, M. A., Nixon, C. A., et al. 2018, *AJ*, **155**, 251
 Teanby, N. A., Irwin, P. G. J., de Kok, R., & Nixon, C. A. 2010, *ApJL*, **724**, L84
 Teanby, N. A., Irwin, P. G. J., Nixon, C. A., et al. 2013, *P&SS*, **75**, 136
 Thelen, A. E., Nixon, C. A., Chanover, N. J., et al. 2018, *Icar*, **307**, 380
 Thelen, A. E., Nixon, C. A., Chanover, N. J., et al. 2019a, *Icar*, **319**, 417
 Thelen, A. E., Nixon, C. A., Cordiner, M. A., et al. 2019b, *AJ*, **157**, 219
 Thompson, W. R., Henry, T. J., Schwartz, J. M., Khare, B. N., & Sagan, C. 1991, *Icar*, **90**, 57
 Vinatier, S., Bézard, B., Fouchet, T., et al. 2007, *Icar*, **188**, 120
 Vuitton, V., Yelle, R. V., Klippenstein, S. J., Hörst, S. M., & Lavvas, P. 2019, *Icar*, **324**, 120
 Vuitton, V., Yelle, R. V., & McEwan, M. J. 2007, *Icar*, **191**, 722
 Wang, J., Ding, Y.-h., & Sun, C.-c. 2006, *ChemPhysChem*, **7**, 710
 Yamaki, H., Kamenno, S., Beppu, H., Mizuno, I., & Imai, H. 2012, *PASJ*, **64**, 118
 Zhu, Z., Zhang, Z., Huang, C., et al. 2003, *JPCA*, **107**, 10288